



The distribution of intervariant crystallographic planes in a lath martensite using five macroscopic parameters

Hossein Beladi^{a,*}, Gregory S. Rohrer^b, Anthony D. Rollett^b, Vahid Tari^c, Peter D. Hodgson^a

^a Institute for Frontier Materials, Deakin University, Geelong, VIC 3216, Australia

^b Department of Materials Science and Engineering, Carnegie Mellon University, Pittsburgh, PA 15213-3890, USA

^c Center for Advanced Vehicular Systems, Mississippi State University, Starkville, MS 39759, USA

Received 16 August 2013; received in revised form 7 October 2013; accepted 7 October 2013

Available online 5 November 2013

Abstract

Electron backscatter diffraction analysis was employed to compute the closest orientation relationship and the distribution of intervariant boundary character in a lath martensitic microstructure. The misorientations were close to the Kurdjumov–Sachs orientation relationship. The intervariant crystallographic plane distribution exhibited a relatively high anisotropy with a tendency for the lath interfaces to terminate on (110) planes. This results from the crystallographic constraints associated with the shear transformation rather than a low energy interface configuration. The lath martensite habit plane was determined to be mostly (110) or near (110). The relative populations of boundaries with [111] and [110] misorientations were greater than other high index misorientations, mostly characterized as (110) symmetric tilt and (110) twist boundary types, respectively. Analysis with homology metrics of the connectivity in the lath martensitic microstructure revealed the connectivity dominated by population of misorientation angle and boundary plane type. © 2013 Acta Materialia Inc. Published by Elsevier Ltd. All rights reserved.

Keywords: Lath martensite; Intervariant plane distribution, Microstructure; Electron backscattering diffraction, Boundary network

1. Introduction

Martensitic steels are widely used in structural sheet applications (e.g. automotive), offering an invaluable combination of mechanical properties, which ultimately reduces the weight of the components and improves safety. Ferrous martensite displays a wide range of morphologies depending upon the composition (e.g. carbon content) such as: lath, butterfly, lenticular and thin plate [1]. Among the different morphologies, the lath martensite, which forms in low carbon steels (i.e. 0.01–0.2 wt.% C), has high industrial significance because of its excellent combination of strength and toughness along with good weldability.

In the lath martensitic phase transformation, the prior austenite grain is typically divided into a three-level

hierarchy in terms of morphology: packet, block and lath. The packet consists of one or several sets of blocks that are individually further subdivided into laths, which are narrow and fine units with a submicron range width [1,2]. The martensitic phase transformation leads to very fine and complex microstructure arrangements, depending on the variant selection mechanism and the orientation relationship between the parent austenite and the martensitic lath formed during the phase transformation. This results in different intervariant interface/boundary character distributions, which may alter the extent of microstructural refinement and consequently the final mechanical properties [3–5].

Grain refinement is the key approach to enhance the strength, reduce the ductile–brittle transition temperature (i.e. decrease cleavage fracture) and increase the resistance to environmental embrittlement (i.e. hydrogen embrittlement). These properties, however, are influenced by

* Corresponding author. Tel.: +61 3 5227 1250; fax: +61 3 5227 1103.
E-mail address: hossein.beladi@deakin.edu.au (H. Beladi).

different crystallographic planes. For instance, cleavage fracture tends to follow {100} planes [4,5], while the {110} planes are normally the slip planes for dislocation glide [4,5] and also control the hydrogen embrittlement [4–6]. An effective grain size can be introduced [5], which should be defined through the microstructural features that correspond to the relevant crystallographic characteristics (i.e. planes) to the problem in hand. The effective grain size, indeed, is a scalar measure of the boundary network structure (i.e. connectivity) for a specific crystallographic plane, which is relevant to the mechanical property of interest. This, therefore, motivates the investigation of the characteristics of the interlath interface/boundary plane distribution in the lath martensitic microstructure to ultimately evaluate the connectivity of specific crystallographic plane/s.

The characterization of the interface/boundary plane character distribution requires five independent parameters, consisting of three parameters describing lattice misorientation and two parameters specifying the boundary plane orientation [7]. The five-parameter interface/boundary character distribution specifies the relative areas of different interface/boundary types and is used to quantify the grain boundary population. The lattice misorientation can be measured using the conventional electron backscatter diffraction (EBSD) technique. However, the two parameters describing the boundary plane orientation must be from a three-dimensional (3-D) measurement of the internal microstructure using transmission electron microscopy (TEM) or serial sectioning in conjunction with EBSD. TEM has been used extensively to examine the intervariant interfaces in lath martensite [8–14]. However, the results were inconclusive or contradictory, probably because only small portions of the microstructure can be studied by TEM. 3-D analysis techniques have also been used to measure the grain boundary distribution, but this has been limited to single phase polycrystalline materials [15–17]. 3-D EBSD has been used to measure the orientation and morphology of coarse martensite, but this study was limited to just a few crystals [18]. 3-D analysis has also been performed for lath martensite, but only to characterize the 3-D morphology of microstructure constituents (e.g. block) [19,20], rather than the intervariant interface plane distribution. This is not surprising, as 3-D techniques are still relatively complex and time consuming.

Recently, a novel approach was developed to statistically measure all five independent boundary parameters using the conventional EBSD orientation mapping technique. The five-parameter analysis approach, which is described in detail elsewhere [7], allows us to specify both the boundary plane orientation distribution and the misorientation distribution. This analysis has been broadly used for ceramic materials [21–23] and metals with different crystal structures [24–26], generally revealing significant anisotropy in the distribution of boundary planes at a given lattice misorientation. The objective of the current work is to provide a detailed description of the intervariant

interface/boundary character distribution in a lath martensitic microstructure formed in a low carbon low alloy steel using the five-parameter grain boundary analysis approach. The intervariant plane connectivity was also analyzed as a function of disorientation angle and boundary plane type (i.e. twist and/or tilt boundaries).

2. Experimental procedure

2.1. Thermomechanical procedure

The composition of the steel was 0.04C–1.52Mn–0.2Si–0.22Mo–0.08Ti–0.033Al (in wt.%). The as-received slab was reduced in thickness by hot rolling from 40 mm to 12 mm thick at temperatures between 1200 and 1000 °C. Two cylindrical compression samples with a length of 15 mm and a diameter of 10 mm were machined out of the hot rolled plate perpendicular to the rolling direction. The samples were reheated at 5 °C s⁻¹ to 1200 °C and held for 20 s. Subsequently, they were compressed to an equivalent strain of 0.5 at 1200 °C at a strain rate of 1 s⁻¹ and held for 60 s. One sample was then immediately water quenched. This thermomechanical procedure was employed to obtain a martensitic microstructure from fully recrystallized austenite grains. Another specimen was cooled at a cooling rate of 10 °C s⁻¹ to 650 °C and held for 10 min to attain a fully ferritic structure. This structure was used to compare the connectivity of the boundary/interface network between the fully martensitic structure and the polygonal ferrite microstructure. The average prior austenite grain size was ~35 µm.

The compression device was a servohydraulic thermo-mechanical treatment simulator apparatus (Servotest, 500 kN) equipped with an automated testing machine including an induction furnace, a muffle furnace and a computer data-acquisition system. Temperature was monitored throughout the testing using a thermocouple embedded into the specimen. A boron nitride lubricant was used to coat the specimen and minimize the friction between the contact surfaces of the specimen and the anvils during deformation.

2.2. EBSD measurement

The deformed specimen was cut from the middle of the hot deformed sample along the deformation direction to analyze the microstructure using EBSD. The sample was prepared by standard mechanical polishing followed by a colloidal silica slurry polish. The EBSD measurements were performed using a field emission gun Quanta 3-D FEI scanning electron microscope operated at 20 kV and 4 nA. The instrument was equipped with a fully automated EBSD device attachment. Data acquisition and post-processing were performed using the TexSEM Laboratories, Inc. software (TSL). Multiple EBSD maps were acquired using a spatial step size of 0.15 µm and 2 µm on a hexagonal grid for the lath martensite and ferritic

microstructures, respectively. The total area covered $\sim 85,000 \mu\text{m}^2$ for the lath martensitic structure. The average confidence index generally varied between 0.62 and 0.71. The lath martensite was assumed to have a crystal structure close to body-centered cubic (bcc) because of the very low carbon content of the steel ($\sim 0.04 \text{ wt.}\%$) [27].

2.3. Determination of the orientation relationship

Because there is no retained austenite in the present martensitic structure at room temperature on quenching, it is impossible to directly measure the orientation relationship (OR) between the lath martensite and parent austenite. In the current study, a novel approach was used to deduce the closest possible OR for the phase transformation from a set of daughter (i.e. martensite) orientation variants and ultimately postulate the parent austenite orientation [28]. Briefly, the variants actually measured originate from a single, unknown parent austenite orientation. This austenite orientation must be a member of each set of possible parent austenite orientations corresponding to each daughter orientation in a given prior austenite grain. Therefore we seek to identify this single parent austenite orientation using different ORs to find the best fit because measurement uncertainty means that there is no single austenite orientation that provides an exact answer. Thus each martensite variant is back-transformed to a set of 24 different potential parent austenite orientations for the Kurdjumov–Sachs (K–S) and Greninger–Troiano (G–T) ORs or 12 for the and Nishiyama–Wassermann (N–W) and Pitsch ORs (see Table 1). Clusters of similar back-transformed austenite orientations are formed, picking one from each set (from each measured variant) through minimizing the sum of the misorientations as each pick is added to the cluster. Finally, the cluster with minimum summation of mutual misorientation angles (SMMAs) is identified as the most probable parent austenite orientation and simultaneously identifies the most probable OR. This analysis requires at least seven different variants to be present in a given prior austenite grain to reliably determine both the possible parent austenite orientation and the closest OR [29].

The TSL software was initially employed to extract the lath orientation for the back-calculation approach. In short, a grain dilation clean-up function was first applied to all orientation maps to eliminate ambiguous data. A single orientation was then assigned to a given grain by

averaging all orientation data belonging to that grain (hereafter called the cleaned EBSD map). The orientations of at least seven distinct variants were extracted for each prior austenite grain to compute the prior austenite orientation and the closest possible OR.

2.4. The intervariant interface/boundary character distribution

A stereological procedure was employed in the current study to measure the intervariant boundary character distribution from the EBSD data [30]. This procedure mainly requires a sufficient number of boundary traces/segments, i.e. the intersection lines between a boundary plane (here two adjacent interface variants) and the plane of observation (i.e. sample surface). The traces are characterized against the lattice misorientation and orientation inside the section plane.

Knowing the crystal/variant orientation, the boundary trace/segment can be transformed to the bicrystal reference frame (Fig. 1). Although it is impossible to determine the orientation of the actual plane for each trace, the plane must be located in the zone of the trace. Therefore, the actual plane belongs to a set of planes whose normals are perpendicular to the line segment (Fig. 1b). Consequently, these planes are located on a great circle perpendicular to the line segment on a stereographic projection (Fig. 1c). The observations of many boundary segments from different crystals/variants with the same misorientation are accumulated in a stereogram such that each segment is represented by its own great circle that is the zone of the trace, Fig. 1c–e. The most important point here is that if there were a single correct habit plane for this misorientation, then we can be certain that it appeared in each set of possible planes. Hence, the great circles arising from each observed line segment must intersect at the position of the correct plane (Fig. 1e). On the other hand, the incorrect planes are observed less frequently in the distribution and are, in effect, a background count that is subtracted from the accumulated stereogram via a simple procedure [30]. The same argument can be extended to the situation where there is a distribution of preferred planes [30]. Therefore, if sufficient traces (e.g. more than 50,000 boundary traces for a cubic system [7]) are collected from the EBSD data, it is possible to determine the most probable orientation of a given boundary/interface plane. The boundary character distribution, $\lambda(\Delta g, \mathbf{n})$, is the relative area of distinguishable

Table 1
Ideal orientation relationships between lath martensite (α) and parent austenite (γ).

Orientation relationship	Parallelism	Minimum angle/axis	Number of variants	Ref.
Bain (B)	$\{100\}_\gamma \parallel \{100\}_\alpha \langle 100 \rangle_\gamma \parallel \langle 110 \rangle_\alpha$	$45^\circ / \langle 100 \rangle$	3	[34]
Kurdjumov–Sachs (K–S)	$\{111\}_\gamma \parallel \{110\}_\alpha \langle 110 \rangle_\gamma \parallel \langle 111 \rangle_\alpha$	$42.85^\circ / \langle 0.968 \ 0.178 \ 0.178 \rangle$	24	[35]
Greninger–Troiano (G–T)	$\{111\}_\gamma \parallel \{110\}_\alpha \langle 123 \rangle_\gamma \parallel \langle 133 \rangle_\alpha$	$44.23^\circ / \langle 0.973 \ 0.189 \ 0.133 \rangle$	24	[36]
Pitsch (P)	$\{100\}_\gamma \parallel \{110\}_\alpha \langle 110 \rangle_\gamma \parallel \langle 111 \rangle_\alpha$	$45.98^\circ / \langle 0.08 \ 0.2 \ 0.98 \rangle$	12	[37]
Nishiyama–Wasserman (N–W)	$\{111\}_\gamma \parallel \{110\}_\alpha \langle 112 \rangle_\gamma \parallel \langle 110 \rangle_\alpha$	$45.98^\circ / \langle 0.976 \ 0.083 \ 0.201 \rangle$	12	[38]

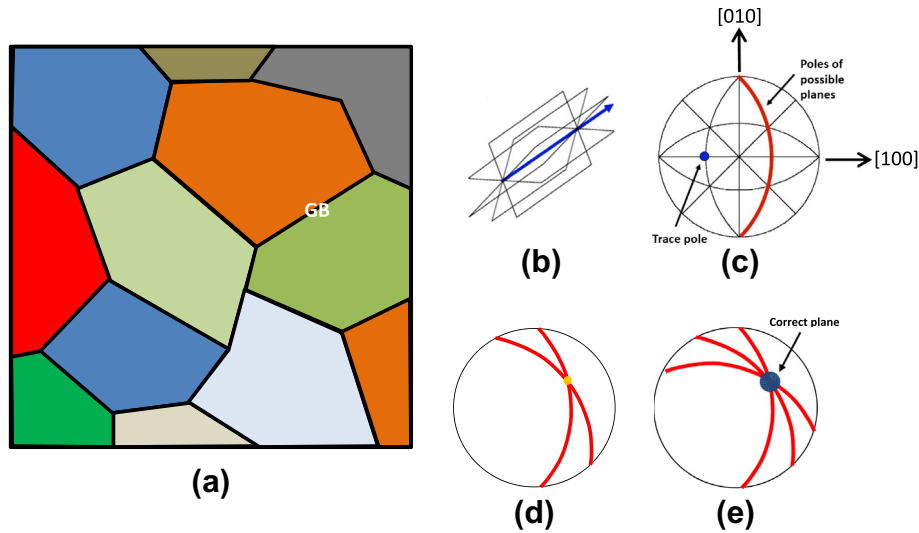


Fig. 1. (a) Schematic representation of stereology approach to analyze the grain boundary plane distribution from two-dimensional EBSD data. (b) The zone axis of possible boundary planes for a given grain boundary (e.g. GB in (a)). (c–e) The transformation of trace of the boundary segment trace into a stereogram in the crystal frame and the accumulation of the associated intensity along the zone of each trace (to represent all the possible normals for that trace), for different numbers of segments: (c) one grain boundary (e.g. GB in (a)), (d) two boundaries and (e) three boundaries.

boundaries characterized by their lattice misorientation (Δg) and boundary plane orientation (\mathbf{n}). It is measured in multiples of a random distribution (MRD), where the values higher than one mean that planes were observed more frequently than expected in a random distribution.

The cleaned EBSD data were also used here to collect the required information for calculating the intervariant plane character distribution. The line traces/segments were extracted after smoothing uneven grain boundaries using the reconstruct grain boundaries function in the TSL software, using a boundary deviation limit of 2 pixels (i.e. 0.3 μm). There were $\sim 930,000$ line traces after excluding the boundary segments of less than 0.45 μm . The line traces indeed included all boundaries/interfaces between packets, blocks and laths. These line traces were employed to calculate the five-parameter boundary character distribution. The analysis was carried out at 9 bins per 90° level of discretization, which offers $\sim 10^\circ$ resolution in the current study. At this resolution 97% of the bins contained at least ten observations.

2.5. Connectivity of interfacial boundary planes

Homology metrics were employed here to measure the connectivity of the boundary networks in plane sections of martensite using two-dimensional EBSD data. These metrics properly represent the boundary network structure [31,32]. Two topological parameters, known as Betti numbers, are required to measure the connectivity of boundary networks: the number of independent pieces of the network (i.e. separate boundary segments referred to as B_0) and the number of closed loops (i.e. enclosed paths of boundaries referred to as B_1) [31,32]. The ratio of B_0/B_1 represents the inverse connectivity of the boundary network structure,

which can be measured as a function of boundary disorientation angle and/or axis. Fig. 2 schematically represents the influence of microstructural characteristics on the inverse connectivity of grain boundary network. An equiaxed grain structure has very low inverse connectivity (Fig. 2a). The number of disconnected boundaries, i.e. B_0 , rises with increases in the disorientation angle threshold, consequently reducing the connectivity of the boundary network (i.e. increasing B_0/B_1 , Fig. 2b and c). The key point here is that the changes in the inverse connectivity as a function of disorientation angle threshold strongly depend on the characteristics of the grain boundary network.

In brief, the cleaned EBSD maps collected on a hexagonal grid were converted to a square grid pattern. The EBSD maps were then computed as a disorientation map, where each pixel has the value of the minimum disorientation angle between that pixel and its eight nearest neighbors in the EBSD map. Afterwards, the topological parameters (i.e. B_0 and B_1) were computed using the software Chomp [33], which is available online for free, to measure the connectivity of the boundary network structure at different disorientation angle thresholds and misorientation axes.

3. Results

The as-quenched microstructure was fully martensitic and consisted of fine laths with high dislocation density (Fig. 3a). Theoretically, each prior austenite grain can transform up to 12 or 24 different orientation variants, depending upon the OR between the parent austenite (i.e. face-centered cubic, fcc) and transformed product (i.e. bcc – e.g. ferrite/martensite). To study the intervariant

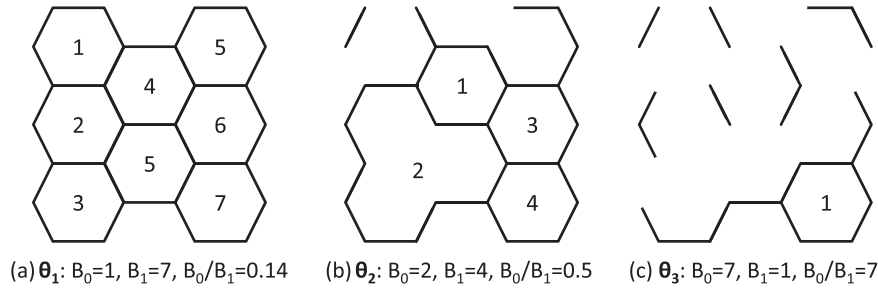


Fig. 2. (a–c) Schematic representation of the inverse connectivity (B_0/B_1) measurement as a function of disorientation angle threshold (θ) where $\theta_1 < \theta_2 < \theta_3$. B_0 measures the number of boundaries not connected to the network and it would be 1 when the network is complete (i.e. (a)). B_1 measures the number of continuous, closed paths of grain boundaries.

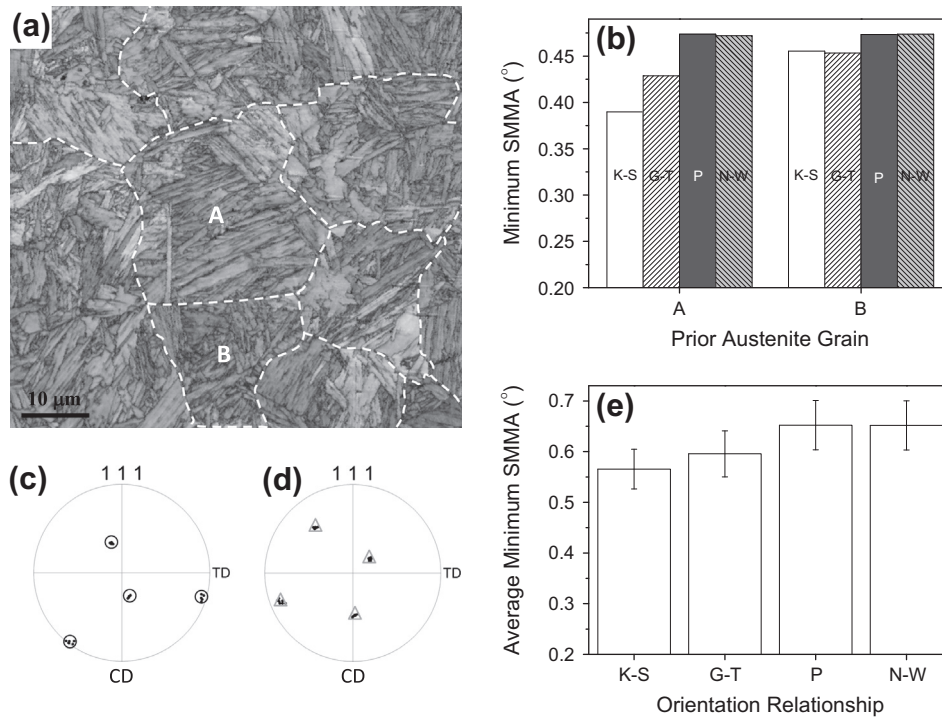


Fig. 3. (a) EBSD map of the lath martensite. Dashed white lines represent prior austenite grain boundaries. (b) The minimum SMMA of prior austenite grains A and B highlighted in (a). (111) pole figures of the grains A (c) and B (d). (e) Average minimum SMMA for different orientation relationships. CD and TD are the compression direction and transverse direction, respectively.

plane character distribution, it is essential to know the closest orientation relationship between the martensite and parent austenite as each OR results in specific sets of intervariant misorientation angle/axis pairs.

3.1. Orientation relationship determination through the back-calculation approach

The OR can ideally be described by one of five major models that specify which crystallographic planes and directions are parallel. These are Bain [34], Kurdjumov–Sachs (K–S) [35], Greninger–Troiano (G–T) [36] Pitch [37] and Nishiyama–Wassermann (N–W) [38] (Table 1). Apart from the Bain OR, which is rarely observed, the other ORs yield similar products.

The analysis of two adjacent prior austenite grains is shown in Fig. 3 using the back-calculation approach. Here, the orientation of each prior austenite grain was individually computed for the closest possible OR (Fig. 3c and d). The current results showed that all grains did not have the same OR and that it can vary from one grain to another. In general, the minimum SMMA changed between the K–S OR and the G–T OR from one prior austenite grain to another, although their minimum SMMA values were very close. For instance, the closest OR is K–S and G–T for grain A and grain B, respectively, based on the minimum SMMA criterion (Fig. 3b). The current result clearly revealed the presence of complexity in the determination of the OR as ideal ORs were never observed and different OR models applied better in different grains.

In practice, the OR between the parent austenite and the transformed products (e.g. martensite) cannot exactly match the theoretical OR models as the transformed products hold the lattice invariant line instead of the parallel closed packed planes/directions relationship. The OR will be governed by the difference between the lattice parameters of the parent austenite and the transformed product [39], which depend on composition. In addition, the formation of a martensitic lath creates stress in the adjacent austenite because of the shear strain associated with the phase transformation. It has been shown that the orientation of austenite can gradually deviate by as much as 5–6° within a given prior austenite grain because of the stress induced through the formation of martensitic lath/s [9]. This emphasizes the complexity of phase transformation, which may locally vary the OR of lath martensite and adjacent austenite. This can also partly explain why the ORs reported for different low alloy steels were not consistent and ranged from K–S to N–W [1,8,9,40–42], which themselves only vary by 5.26°. Furthermore, the diverse ORs reported for low alloy martensitic steels by different groups might also arise from the fact that the previous reports mainly used TEM and examined only a small portion of microstructure because of the limits on the field of view and the time required for the observations.

Thanks to the EBSD technique and the recent computational advances, the ORs of a large number of grains have been surveyed in the current study, and this makes the conclusions more statistically representative. Here, the minimum SMMA for 25 distinct prior austenite grains were computed using the back-calculation approach. On average, it was revealed that the K–S OR had the minimum SMMA (Fig. 3e) compared with other main orientation relationships. This suggests that the orientation relationship was, on average, very close to the K–S for the current martensitic phase transformation.

3.2. Intervariant plane character distribution analysis

In the case of the K–S OR, 24 crystallographic variants can be formed from a single austenite grain because of the symmetry of cubic systems as listed in Table 2. By comparing all 24 variants, 23 misorientation angle/axis sets can be computed (Table 2). Some of these intervariant interfaces are identical because of crystal symmetry (e.g. V1–V3 and V1–V5), as reported earlier by others [43]. Therefore, the comparison of all 24 variants in the case of K–S OR reduces to only 16 independent misorientations. Consequently, the misorientation angle distribution of martensite was quantitatively different from that of the fully polygonal ferritic structure (Fig. 4a and b). It had a bimodal distribution showing two peaks at low (i.e. ~10–15°) and high (i.e. ~50–60°) misorientation angle ranges. This would be expected as the possible intervariant misorientation angles for the K–S OR are located within these ranges (Table 2). Indeed, the low misorientation angle population approxi-

Table 2

Possible 24 variants generated through phase transformation having a K–S orientation relationship.

Variant	Plane parallel	Direction parallel	Rotation angle/axis from V1
V1	(111) _y (011) _x	[−101] _y [−1−11] _x	–
V2		[−101] _y [−11−1] _x	60°/[11−1]
V3		[01−1] _y [−1−11] _x	60°/[011]
V4		[01−1] _y [−11−1] _x	10.53°/[0−1−1]
V5		[1−10] _y [−1−11] _x	60°/[0−1−1]
V6		[1−10] _y [−11−1] _x	49.47°/[011]
V7	(1−11) _y (011) _x	[10−1] _y [−1−11] _x	49.47°/[−1−11]
V8		[10−1] _y [−11−1] _x	10.53°/[11−1]
V9		[−1−10] _y [−1−11] _x	50.51°/[−103−13]
V10		[−1−10] _y [−11−1] _x	50.51°/[−7−55]
V11		[011] _y [−1−11] _x	14.88°/[1351]
V12		[011] _y [−11−1] _x	57.21°/[−356]
V13	(−111) _y (011) _x	[0−11] _y [−1−11] _x	14.88°/[5−13−1]
V14		[0−11] _y [−11−1] _x	50.51°/[−55−7]
V15		[−10−1] _y [−1−11] _x	57.21°/[−6−25]
V16		[−10−1] _y [−11−1] _x	20.61°/[11−11−6]
V17		[110] _y [−1−11] _x	51.73°/[−116−11]
V18		[110] _y [−11−1] _x	47.11°/[−24−1021]
V19	(11−1) _y (011) _x	[−110] _y [−1−11] _x	50.51°/[−31310]
V20		[−110] _y [−11−1] _x	57.21°/[36−5]
V21		[0−1−1] _y [−1−11] _x	20.61°/[30−1]
V22		[0−1−1] _y [−11−1] _x	47.11°/[−102124]
V23		[101] _y [−1−11] _x	57.21°/[−2−5−6]
V24		[101] _y [−11−1] _x	21.06°/[9−40]

mately in the range of 20°–40° represents the misorientation angles inherited from the prior austenite grain boundaries.

Variants can be classified into four distinct crystallographic packets in a given prior austenite grain. The laths in a specific packet have the same close-packed planes parallel (i.e. habit plane, e.g. V1–V6, Table 2). It appeared that most intervariant boundary fractions belonged to the laths from the same crystallographic packet. Based on the microstructure observations, Fig. 4c shows the frequency with which the different variants are adopted. It is worth noting that the V1–V6 intervariant interface was relatively low compared with other interfaces, even though they belong to the same crystallographic packet (Fig. 4c). In general, interfaces that form as a result of the intersection of two distinct crystallographic packets were observed less frequently. The intervariant boundary fraction of the lath martensite mostly exhibited larger fractions than the polygonal ferritic structure transformed from recrystallized austenite.

The distribution of intervariant planes independent of misorientation, $\lambda(\mathbf{n})$, where \mathbf{n} is the normal to the intervariant boundary, was anisotropic, and exhibits a maximum at the (101) position with a value of 1.71 MRD (Fig. 5). In other words, the population was 71% greater than expected in a random distribution, suggesting that most intervariant interfaces were terminated on (101) planes. The minimum of the distribution was centered at (100) with 0.51 MRD

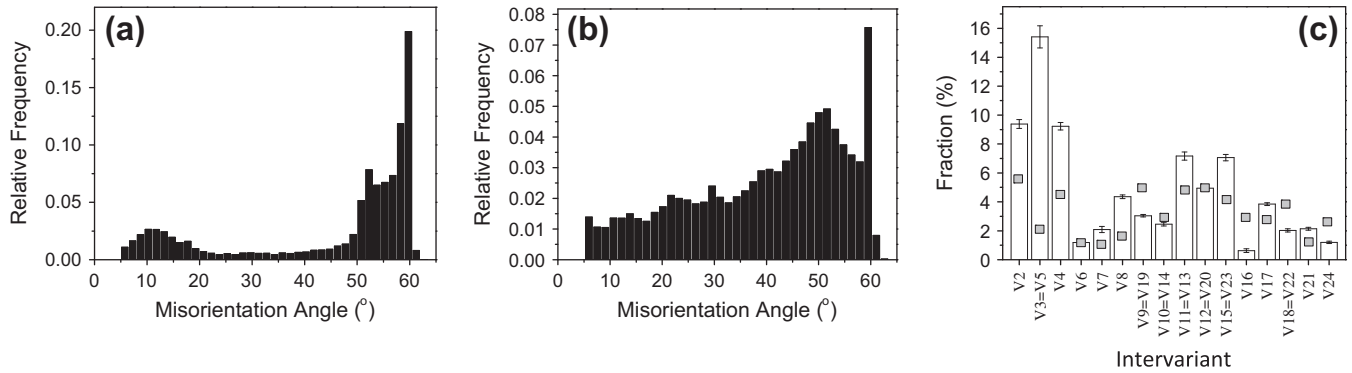


Fig. 4. Misorientation angle distribution for fully martensitic (a) and polygonal ferritic (b) microstructures. (c) The fraction of total population of interfaces that belong to K–S OR, comparing intervariant interfaces between V1 and V_i ($i = 2–24$) for the martensite (i.e. column) and polygonal ferrite (i.e. square). The highest fraction of interfaces belongs to the same crystallographic packet (V1 to V5). Because of symmetry, there are only 16 independent intervariant interfaces and the “=” sign shows two equivalent intervariant interfaces.

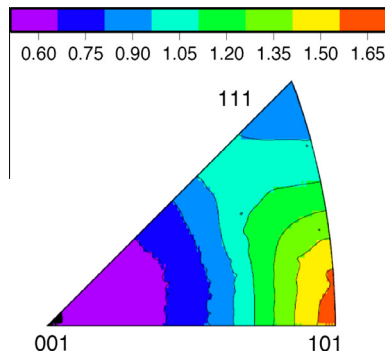


Fig. 5. The distribution of boundary planes of the lath martensitic steel. The contour values are in MRD, which is multiples of a random distribution.

(Fig. 5). The distribution was ~ 0.9 MRD at the (111) position.

The intervariant plane distributions were plotted for specific misorientations about [111] and [110] related to the K–S OR, using five macroscopic boundary parameters (Figs. 6 and 7). Other misorientation angle/axis pairs associated with the K–S OR listed in Table 2 were also computed (Fig. 8). In general, there were significant changes in the distribution of intervariant planes as a function of misorientation angle for both misorientation axes of [111] and [110].

A schematic stereogram for the projection was plotted for the $[11-1]$ misorientation axis to highlight the position of the plane normal associated with twist boundaries (i.e. the interface plane normal is parallel to the misorientation axis) and tilt boundaries as the zone of normals perpendicular to the misorientation axis, Fig. 6a. For a $[111]$ misorientation axis, the distributions showed multiple peaks mainly centered on the zone axis of the tilt boundaries (i.e. the great circle perpendicular to the $[11-1]$ or $[-1-11]$ axes, Fig. 6b–d. Twist boundaries were absent, as evident from the lack of intensity at the $(11-1)$ twist boundary position, Fig. 6b–d. The peak distributions were

slightly strengthened up to the misorientation angle of 49.5° with intensities ~ 9 MRD, Fig. 6b and c. At the misorientation angle of 60° , the peaks were much stronger and mainly centered at the $\{110\}||\{110\}$ symmetric boundary positions (i.e. the surfaces on either side of the boundary are the same) with ~ 74 MRD, Fig. 6d.

The $[101]$ misorientation axis revealed a similar trend with respect to the misorientation angle (Fig. 7). At a misorientation of 10.53° , the populations were centered at different $\{110\}$ positions with ~ 7.7 MRD (Fig. 7a). The distribution significantly strengthened at the next misorientation angle of 49.47° , where only a single peak appeared at the twist boundary position of $\{110\}||\{110\}$ with ~ 13.7 MRD (Fig. 7b). The characteristics of the distribution were similar at 60° , though the population was substantially enhanced at the (011) twist boundary position to ~ 123 MRD (Fig. 7c).

The distributions of other high index misorientations listed in Table 2 are presented in Fig. 8. They mostly showed either a single peak or multiple peaks almost centered at the $\{110\}$ positions. In other words, these intervariant interfaces were mainly terminated at $\{110\}$ or near $\{110\}$ planes, though these planes did not have pure tilt or twist type characteristics (Fig. 8). Finally, it should be noted that the relative population of boundaries with $[110]$ and $[111]$ misorientations were significantly greater than other high index misorientations.

Fig. 9 shows the twist boundaries population for all misorientation axes along the edges of the standard stereographic triangle. The horizontal lines for each misorientation axis represent the population of twist boundaries as a function of twist angle. The intensity of the population was plotted on a natural log scale (MRD + 1). The peaks observed in Fig. 9 can be closely linked to the intervariant plane distributions shown in Figs. 6–8. The multiple peaks with moderate intensity appearing on the left-hand side of the plot represent low misorientation angle boundaries (i.e. $\omega < 15^\circ$). There were also two moderately high populations at 180° about the

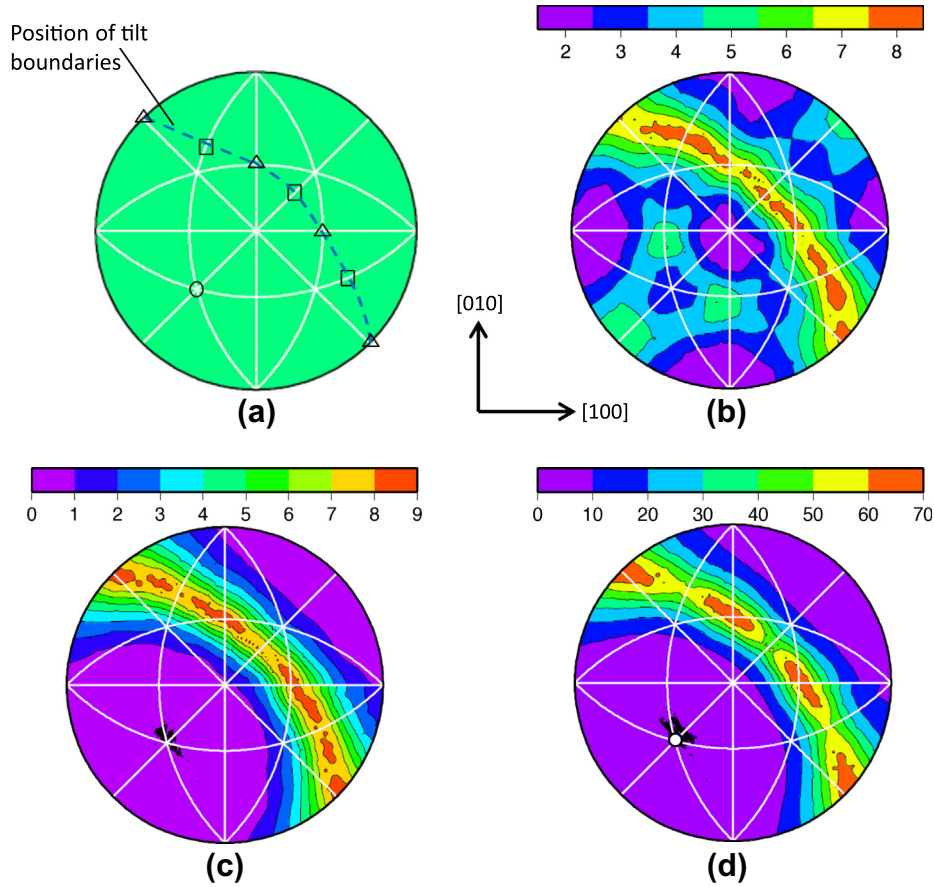


Fig. 6. (a) Schematic representation of the position of different boundary types in the grain boundary plane distributions around the $[11\bar{1}]$ axis. Square, triangle and circle marks in (a) represent the position of $\{112\}$ and $\{110\}$ symmetric tilt and $\{111\}$ twist boundaries, respectively. (b–d) The distribution of boundary plane normals for boundaries with different misorientations around $[11\bar{1}]$ axis: (b) $10.53^\circ/[11\bar{1}]$, (c) $49.47^\circ/[\bar{1}\bar{1}1]$, (d) $60^\circ/[11\bar{1}]$. The contour values are in MRD. Here, the $[001]$ crystal axis is positioned perpendicular to the paper plane and the $[100]$ direction located horizontally in the plane of the paper to the right.

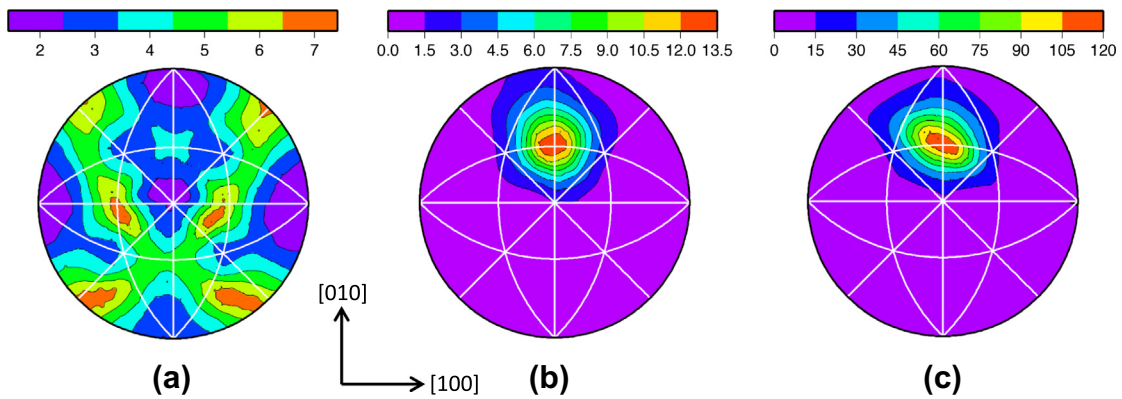


Fig. 7. The distribution of boundary plane normals for boundaries with different misorientations around $[011]$ axis: (a) $V1-V4 = 10.53^\circ/[0\bar{1}\bar{1}]$, (b) $V1-V6 = 49.47^\circ/[011]$, (c) $V1-V3/V1-V5 = 60^\circ/[011]$. The contour values are in MRD.

$\langle 110 \rangle$ axis corresponding to low misorientation angles. The peaks between $[\bar{1}11]$ and $[\bar{3}11]$ at 180° and 140° can be referred to as $\{u11\}$ twist boundaries. There were also multiple peaks about $[110]$ at misorientation angles of 60° and 120° . The former was very close to the intervariant misorientation angle/axis of $V1-V3$ and

$V1-V5$ (i.e. $60^\circ/[011]$). The latter is symmetrically indistinguishable from the misorientations in the fundamental zone and it was very close to $V1-V6$ intervariant boundaries (i.e. $49.5^\circ/[011]$). The twist boundaries about the $[110]$ twist axis had greater populations than those along other twist axes.

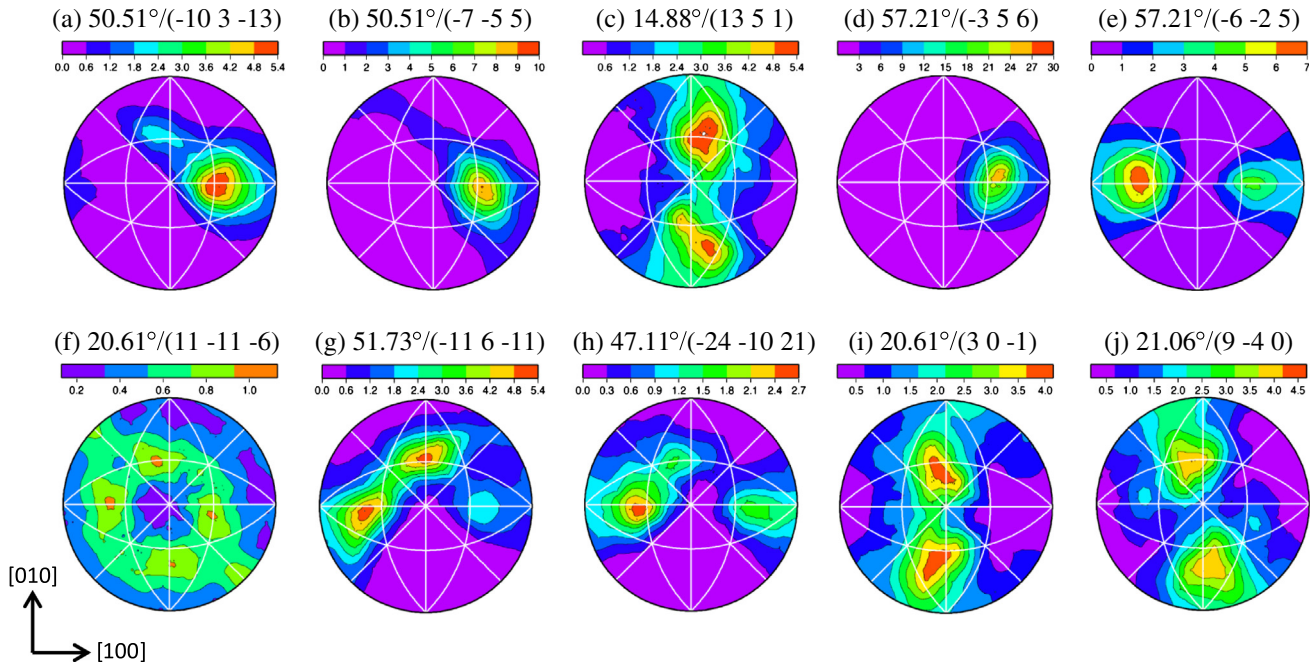


Fig. 8. The distribution of grain boundary plane normals for boundaries with different misorientation angles and axes. The contour values are in MRD.

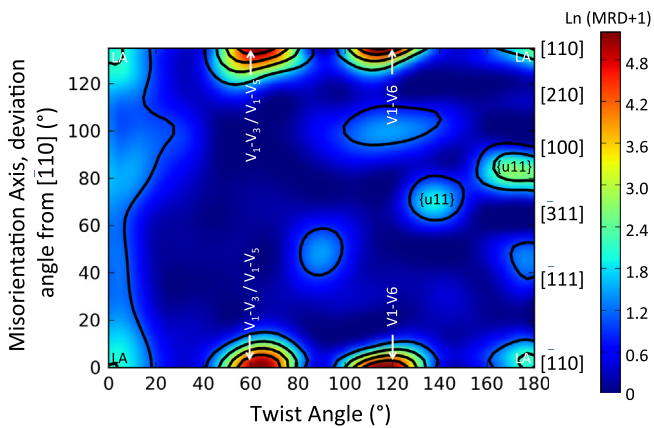


Fig. 9. Twist boundaries for all misorientation axes on the edges of the standard stereographic triangle. LA represents the positions of low misorientations.

3.3. Connectivity of boundary network

Fig. 10 shows the inverse connectivity of the boundary network (B_0/B_1) as a function of disorientation angles for the martensitic structure in comparison with the polygonal ferritic microstructure using the homology metrics approach. As one might expect, the boundary network becomes less connected for both microstructures as the threshold disorientation angle increases (i.e. eliminating more boundaries from the network below the threshold value, Fig. 10a–i). This caused a continuous increase in B_0/B_1 with disorientation angle for both microstructures. However, there was a distinct difference in the rate of connectivity change for the martensitic structure compared with the fully ferritic structure (Fig. 10i). The latter initially

revealed a small slope and then increased continuously from 10° to ~50°, above which the rate became slower. On the other hand, the martensitic structure revealed negligible change in the inverse connectivity at a disorientation angle range of 20 to 40° (i.e. referring to the disorientation angle originated from the prior austenite grain boundaries) and then increased continuously. In general, the martensitic microstructure appeared less connected below 30° and then its boundary network connectivity significantly increased compared with the ferritic structure (Fig. 10i).

4. Discussion

The results presented here comprise the first comprehensive characterization of the intervariant boundary/interface character distribution of lath martensite microstructure using five independent crystallographic boundary parameters. Because the properties of lath martensitic microstructures (cleavage fracture, hydrogen embrittlement, plasticity) are influenced by the orientations of the intervariant planes, these distributions can be used to increase our knowledge of structure–property relations.

4.1. Intervariant plane character distribution

The intervariant boundary planes have {110} normals more frequently than any other plane orientations in the lath martensitic structure when the misorientation is ignored. For instance, the frequency of {110} planes is more than three times greater than that of the {100} planes, suggesting relatively high anisotropy in the intervariant plane distribution (Fig. 5). Although low carbon martensite has a crystal structure close to bcc [27], the

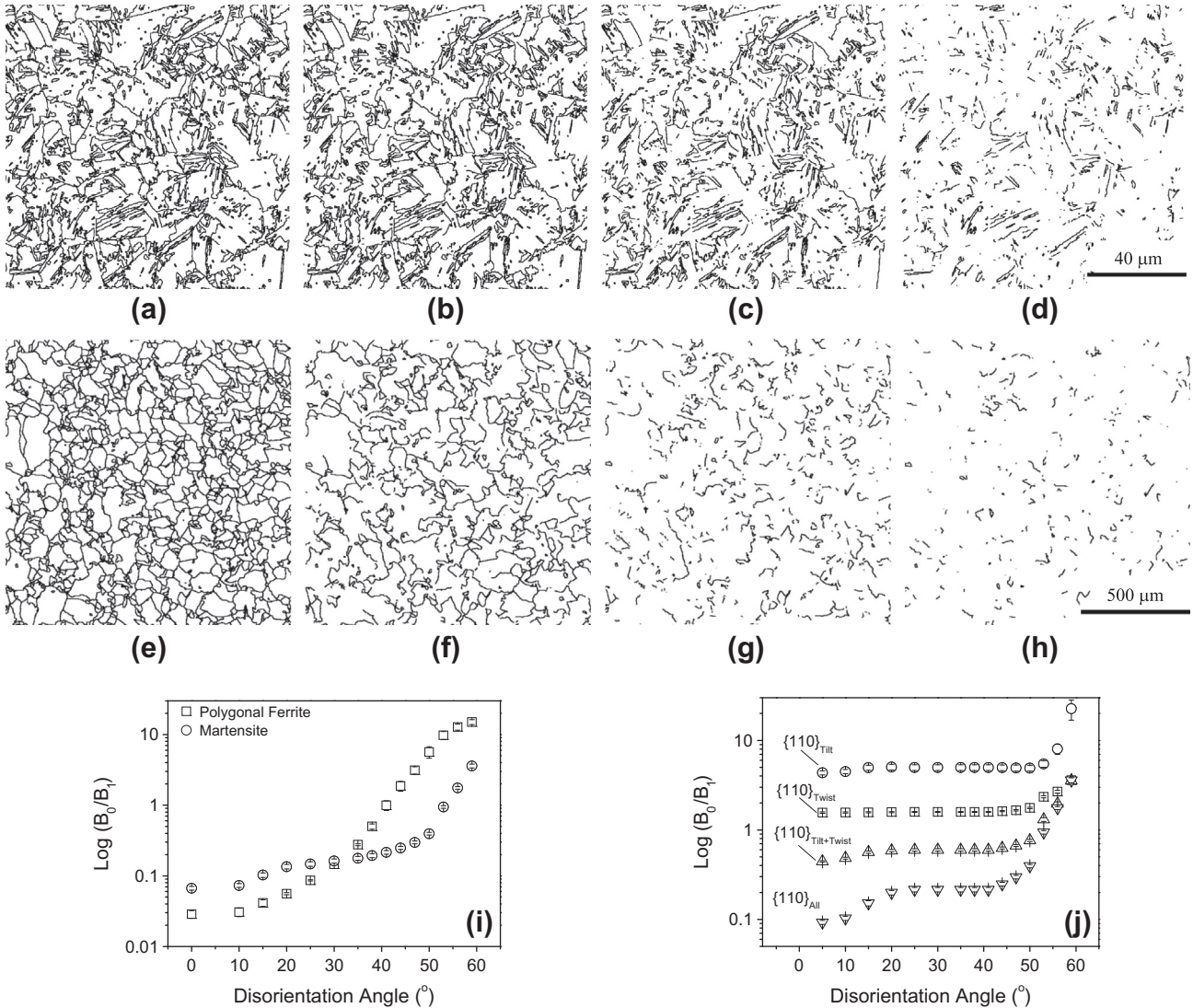


Fig. 10. Thresholded boundary maps for the lath martensite (a–d) and polygonal ferrite (e–h) microstructures for all boundaries with disorientation angle (a, e) $>20^\circ$, (b, f) $>41^\circ$, (c, g) $>53^\circ$, (d, h) $>59^\circ$. The inverse connectivity of boundary network structure as a function of disorientation angle threshold for different microstructures (i) and $\{110\}$ plane types (j) for lath martensite microstructure.

current observation is not, however, consistent with the results recently reported for metals with bcc crystal structure having different compositions [17,24,26]. For a Fe–1% Si alloy, the distribution had very little anisotropy, exhibiting the minimum and maximum frequency on the $\{111\}$ and $\{110\}$ planes, respectively [24]. By contrast, the distribution for an interstitial-free (IF) steel with strong $\langle 111 \rangle \parallel \text{ND}$ texture had relatively high anisotropy displaying the highest and lowest populations centered on the $\{111\}$ and $\{100\}$ planes, respectively [26].

The grain boundary population can be influenced by the grain boundary energy, the texture, the grain shape or the transformation path [44]. In microstructures produced by normal grain growth, the grain boundary population is expected to be inversely correlated to the grain boundary energy for a given composition [45]. The relative grain boundary area and energy of a fully ferritic structure with

the same alloying composition to the current martensitic structure was recently measured using focused ion beam serial sectioning combined with EBSD [17]. Interestingly, there was a strong inverse correlation between the relative areas of different types of grain boundaries and the relative grain boundary energies. However, the grain boundary character distribution differs significantly from the current martensitic structure. The distribution was similar to a previously analyzed IF steel, where the minima and maxima were centered on the $\{111\}$ and $\{100\}$ planes, respectively. There was also very little anisotropy in the grain boundary plane distribution of the fully ferritic steel, which had a weaker $\langle 111 \rangle \parallel \text{ND}$ texture compared with the IF steel. Therefore, the difference between the previous analysis [17] and the current result cannot be the result of differences in the grain boundary energy, because the two materials had identical compositions. This suggests that the

observed changes in the martensitic structure are mainly related to the processing (i.e. texture and phase transformation). The martensitic microstructure transformed from fully recrystallized austenite that had a relatively weak texture that should not by itself impart strong texture on the transformed product [46]. To explain the strong anisotropy in the boundary plane distribution of the martensitic structure, it would therefore be necessary to examine the effect of the martensitic phase transformation mechanism on the interface/boundary plane development.

During a shear phase transformation (e.g. martensite), there is a strong crystallographic relationship between the parent austenite and the product (i.e. lath martensite), which may follow one of the ideal orientation relationships listed in Table 1. These ORs match the close-packed planes of lath martensite and the adjacent austenite (i.e. $\{111\}_\gamma \parallel \{110\}_\alpha$). Here, the OR of lath martensite was, on average, shown to be close to the K–S OR using the back-calculation approach (Fig. 3). The main difference between the ideal orientation relationships is the orientation of crystallographic directions in the interface plane (see Table 1). Considering the crystallographic constraint of the shear transformation, it would be expected that two adjacent martensite laths will, most likely, impinge on $\{110\}$ planes after the completion of the phase transformation. This is consistent with the current observation, where the highest fraction of interfaces terminates at $\{110\}$ planes irrespective of the misorientation angle (Fig. 5).

Interestingly, the current result clearly shows that a relatively large fraction of lath interfaces (i.e. $\sim 10\%$) exhibit twin orientations (i.e. $V_1 - V_2 = 60^\circ/[1-11] = \Sigma 3$, Fig. 4c), which is much higher than that reported for a polygonal ferritic structure (i.e. 2.5–3% [17,26]). Also the distribution of $\Sigma 3$ interface/boundary normals for martensite is different from those observed in polygonal ferritic microstructure (i.e. bcc lattice structure), although the plane distribution is located on the zone of the misorientation axis, i.e. pure tilt boundaries for both microstructures [17,26]. The main difference is that the maxima are centered on the symmetric $\{110\}$ tilt interfaces/boundaries in the martensitic structure (Fig. 6d), while the maxima are centered on the symmetric $\{112\}$ tilt boundaries (i.e. the coherent twin boundaries in bcc crystal structure [47]) in the polygonal ferritic microstructure [17,26]. The latter is consistent with the grain boundary energy distribution in a ferritic structure, where the symmetric $\{112\}$ tilt boundaries revealed a much lower energy than $\{110\}$ [17]. As discussed earlier, this difference can arise from the crystallographic constraints associated with the shear transformation mainly promoting the $\{110\}$ planes during the martensitic phase transformation, which may not necessarily be the energetically favorite configuration.

The relative orientation of adjacent martensitic laths in a packet has been a matter of discussion among different research groups. Some groups have shown that the adjacent laths sometimes exhibit twin-related orientations

[8–11,14], while others observed that the laths had small misorientations $2\text{--}3^\circ$ rather than being twin-related [48,49]. The discrepancy may arise from the fact that not all packets necessarily display the twin-related laths and that the fraction of packets showing the twin-related orientation may vary with the alloy composition as Mn, for instance, enhances the twin-related interfaces [50]. It was shown that the twin-related laths have shear components with exactly opposite shape strains, which cancel each other and consequently promote the shear phase transformation [8]. It was further revealed that the twin-related laths share the same habit plane and long direction [9]. The current result reveals that the habit planes of twin-related laths (i.e. $\Sigma 3$) lay on the zone axis of tilt boundaries, having the maxima on $\{110\}$ planes (i.e. symmetric tilt boundary, $\{110\} \parallel \{110\}$, Fig. 6d). This is consistent with the most measured habit planes of lath martensite reported in the literature. Using TEM, the lath martensite habit plane was determined to be $\{110\}$ [8–11], near $\{110\}$ [12], $\{541\}$ [13], $\{321\}$ [14] and $\{331\}$ [11]. Interestingly, most of these orientations (except $\{331\}$) lay on the zone axis of tilt boundaries (the great circle perpendicular to $[11-1]$ axis, Fig. 6a). The discrepancies in the measured habit planes among the different groups could be a result of the limited areas that were examined, which is a general limitation of TEM. It is important to emphasize that the present analysis, though, results from a large area of the microstructure covering more than 50 prior austenite grains, which provides statistically sound observations.

4.2. Connectivity of boundary/plane network

The inverse connectivity of the boundary network (B_0/B_1) as a function of disorientation angles clearly shows a distinct difference between the martensitic structure and the fully ferritic structure (Fig. 10i). Generally, the boundary network of the martensitic microstructure is less connected below a threshold of 30° in disorientation and then the connectivity is significantly higher by comparison with the ferritic structure (Fig. 10i). This result is not surprising as these changes clearly reflect the distinct difference in the misorientation angle distribution of these microstructures (Fig. 4a and b). Although the current result provides valuable information regarding the connectivity of invariant boundary network in the lath martensite structure, it does not clearly reflect the connectivity of a given crystallographic plane, which can directly govern the mechanical properties.

The invariant interface/boundary character distribution reveals an interesting trend in the lath martensite, which can direct us to measure the connectivity of specific crystallographic plane (i.e. $\{110\}$, Figs. 5–8). The interfaces/boundaries having one of the K–S orientation angle/axis (Table 2) are mostly terminated on $\{110\}$ or near $\{110\}$ planes (Figs. 6–8). Therefore, if the boundaries with disorientation angles in a range of $20\text{--}40^\circ$ (i.e. prior austenite grain boundaries) are excluded from the

microstructure, the connectivity of $\{110\}$ planes can be measured approximately as a function of disorientation angle. Similarly, the distribution of boundaries with a misorientation axis of $[111]$ and $[110]$ shows that they mainly have $\{110\}$ symmetric tilt and $\{110\}$ twist plane types, respectively. This leads to a measure of the connectivity of specific $\{110\}$ plane type/s (i.e. twist and/or tilt boundaries, Fig. 10j). The results clearly show a similar connectivity trend as a function of disorientation angle for different $\{110\}$ types, though the tilt symmetric boundaries have the least connectivity for all disorientation angle thresholds, indicating that $\{110\}$ tilt segments tend to be isolated. The (inverse) connectivities of the different $\{110\}$ type boundaries converge beyond 50° , except for tilt boundaries (Fig. 10j). These changes are clearly reflected in the fraction of the intervariant interface/boundaries (Fig. 4c).

The $\{110\}$ planes are known to govern the dislocation plasticity (i.e. strength) [4,5] and also control the hydrogen embrittlement [4–6]. Therefore, the current results strongly suggested the value of measuring the connectivity of the $\{110\}$ interface/boundary plane network, which, for instance, affects the fracture behavior in materials subjected to the hydrogen embrittlement environment.

5. Conclusions

Based on orientation mapping of a lath martensite microstructure formed from austenite, the K–S OR provides the best explanation for the variants that formed in the majority of the prior austenite grains. The intervariant interface/boundary character distribution in the lath martensite revealed a relatively high anisotropy, mostly terminating on (110) planes. This results from the crystallographic constraints associated with the shear transformation rather than from a low energy interface configuration. The habit planes of lath martensite were shown to be mostly (110) or near (110) planes. The distribution of intervariant interfaces with the misorientation axis of $[111]$ and $[110]$ are mostly centered on $\{110\}$ symmetric tilt and $\{110\}$ twist positions, respectively. The current result ultimately led us to evaluate the connectivity of specific crystallographic planes (i.e. $\{110\}$) as a function of disorientation angle and boundary plane type (i.e. twist and/or tilt boundaries) using homology metrics.

Acknowledgements

Extensive discussions with Prof. Bevis Hutchinson are gratefully acknowledged. The work at Deakin University was supported through the grants provided by the Australian Research Council. The work at Carnegie Mellon University was supported by the MRSEC program of the National Science Foundation under Award Number DMR-0520425 and by the Office of Naval Research under Grant N00014-11-1-0678.

References

- [1] Morito S, Tanaka H, Konishi R, Furuhashi T, Maki T. *Acta Mater* 2003;51:1789.
- [2] Maki T, Tsuzaki K, Tamura I. *Trans ISIJ* 1980;20:207.
- [3] Kim HJ, Kim YH, Morris Jr JW. *ISIJ Int* 1998;38:1277.
- [4] Morris Jr JW, Guo Z, Krenn CR, Kim YH. *ISIJ Int* 2001;41:599.
- [5] Guo Z, Lee CS, Morris Jr JW. *Acta Mater* 2004;52:5511.
- [6] Shibata A, Takahashi H, Tsuji N. *ISIJ Int* 2012;52:208.
- [7] Rohrer GS, Saylor DM, El Dasher B, Adams BL, Rollett AD, Wynblatt P. *Z Metallkd* 2004;95:197.
- [8] Kelly PM, Jostons A, Blake RG. *Acta Metall Mater* 1990;38:1075.
- [9] Kelly PM. *Acta Metall* 1965;13:635.
- [10] Biswas MGA, Codd I. *J Iron Steel Inst* 1968;206:494.
- [11] Thomas G, Rao VVN. *Proc Int Conf Martensite ICOMAT-77 Kiev, U.S.S.R.*; 1978. p. 57.
- [12] Duflos F, Cantor B. *Acta Metall* 1982;30:323.
- [13] Van Gent A, Van Doorn FC, Mittemeijer EJ. *Metall Trans A* 1985;16:1371.
- [14] Chilton JM, Barton CJ, Speich GR. *J Iron Steel Inst* 1970;208:184.
- [15] Dillon SJ, Rohrer GS. *J Am Ceram Soc* 2009;92:1580.
- [16] Li J, Dillon SJ, Rohrer GS. *Acta Mater* 2009;57:4304.
- [17] Beladi H, Rohrer GS. *Acta Mater* 2013;61:1404.
- [18] Rowenhorst DJ, Gupta A, Feng CR, Spanos G. *Scripta Mater* 2006;55:11.
- [19] Morito S, Adachi Y, Ohba T. *Mater Trans* 2009;50:1919.
- [20] Morito S, Edamatsu Y, Ichinotani K, Ohba T, Hayashi T, Adachi Y, et al. *J Alloys Compd*, 2013. doi: <http://dx.doi.org/10.1016/j.jallcom.2012.02.015> [in press].
- [21] Saylor DM, El Dasher BS, Sano T, Rohrer GS. *J Am Ceram Soc* 2004;87:670.
- [22] Saylor DM, El Dasher BS, Pang Y, Miller HM, Wynblatt P, Rollett AD, et al. *J Am Ceram Soc* 2004;87:724.
- [23] Saylor DM, Morawiec A, Rohrer GS. *Acta Mater* 2003;51:3675.
- [24] Bennett TA, Kim CS, Rohrer GS, Rollett AD. *Mater Sci Forum* 2004;467–470:1057.
- [25] Saylor DM, El Dasher BS, Rollett AD, Rohrer GS. *Acta Mater* 2004;52:3649.
- [26] Beladi H, Rohrer GS. *Metall Mater Trans A* 2013;44:115.
- [27] Roberts CS. *J Metals* 1953;5:203.
- [28] Tari V, Rollett AD, Beladi H. *J Appl Cryst* 2013;46:210.
- [29] Humbert M, Blaineau P, Germain L, Gey N. *Scripta Mater* 2011;64:114.
- [30] Saylor DM, El-Dasher BS, Adams BL, Rohrer GS. *Metall Mater Trans A* 2004;35:1981.
- [31] Wanner T, Fuller Jr ER, Saylor DM. *Acta Mater* 2010;58:102.
- [32] Rohrer GS, Miller HM. *Acta Mater* 2010;58:3805.
- [33] Kalies W, Pilarczyk P. Computational homology program; 2004. <<http://www.chomp.rutgers.edu/>>.
- [34] Bain EC. *Trans AIME Steel Division* 1924;79:25.
- [35] Kurdjumov G, Sachs G. *Z Phys* 1930;64:225.
- [36] Greninger AB, Troiano AR. *J Met Trans* 1949;185:590.
- [37] Pitsch W. *Acta Metall* 1962;10:897.
- [38] Nishiyama Z. *Sci Rep Res Inst, Tohoku University* 1934–35, vol. 23. p. 638.
- [39] Christian JW. *Metal Trans A* 1990;21:799.
- [40] Law NC, Howell PR, Edmonds DV. *Metal Sci J* 1979;13:507.
- [41] Rao BVN. *Metall Trans A* 1979;10:645.
- [42] Hutchinson B, Hagstrom J, Karlsson O, Lindell D, Tornberg, Lindberg F, et al. *Acta Mater* 2011;59:5845.
- [43] Gourgues AF, Flower HM, Lindley TC. *Mater Sci Technol* 2000;16:26.
- [44] Randle V, Rohrer GS, Hu Y. *Scripta Mater* 2008;58:183.
- [45] Rohrer GS. *J Mater Sci* 2011;46:5881.
- [46] Ray RK, Jonas JJ, Butron-Guillen MP, Savoie J. *ISIJ Int* 1994;34:927.

- [47] Hirth JP, Lothe J. Theory of dislocations. 2nd ed. Malabar (FL): Krieger; 1982. p. 366.
- [48] Bolton JD, Petty ER. Metal Sci J 1971;5:166.
- [49] Wakasa K, Wayman CM. Acta Metall 1981;29:991.
- [50] Huang D-H, Thomas G. Met Trans 1971;2:1587.